Interaction of the tetratricopeptide repeat domain of aryl hydrocarbon receptor–interacting protein–like 1 with the regulatory Pγ subunit of phosphodiesterase 6

Received for publication, August 15, 2019, and in revised form, September 3, 2019 Published, Papers in Press, September 5, 2019, DOI 10.1074/jbc.RA119.010666

Ravi P. Yadav[‡], Kimberly Boyd[‡], Liping Yu[§¶], and Nikolai O. Artemyev[‡‖1]

From the Departments of [‡]Molecular Physiology and Biophysics, [§]Biochemistry, and [‖]Ophthalmology and Visual Sciences and the [¶]NMR Core Facility, University of Iowa Carver College of Medicine, Iowa City, Iowa 52242

Edited by Wolfgang Peti

Phosphodiesterase-6 (PDE6) is key to both phototransduction and health of rods and cones. Proper folding of PDE6 relies on the chaperone activity of aryl hydrocarbon receptor–interacting protein–like 1 (AIPL1), and mutations in both PDE6 and AIPL1 can cause a severe form of blindness. Although AIPL1 and PDE6 are known to interact via the FK506-binding protein domain of AIPL1, the contribution of the tetratricopeptide repeat (TPR) domain of AIPL1 to its chaperone function is poorly understood. Here, we demonstrate that AIPL1–TPR interacts specifically with the regulatory Pγ subunit of PDE6. Use of NMR chemical shift perturbation (CSP) mapping technique revealed the interface between the C-terminal portion of Pγ and AIPL1–TPR. Our solution of the crystal structure of the AIPL1–TPR domain provided additional information, which together with the CSP data enabled us to generate a model of this interface. Biochemical analysis of chimeric AIPL1–AIP proteins supported this model and also revealed a correlation between the affinity of AIPL1–TPR for Pγ and the ability of Pγ to potentiate the chaperone activity of AIPL1. Based on these results, we present a model of the larger AIPL1–PDE6 complex. This supports the importance of simultaneous interactions of AIPL1–FK506 – binding protein with the prenyl moieties of PDE6 and AIPL1–TPR with the Pγ subunit during the folding and/or assembly of PDE6. This study sheds new light on the versatility of TPR domains in protein folding by describing a novel TPR-protein binding partner, Pγ, and revealing that this subunit imparts AIPL1 selectivity for its client.

Cyclic nucleotide phosphodiesterases of the sixth family (PDE6)[2] are the key effectors in the visual transduction cascade in rod and cone photoreceptors (1, 2). In the dark, activity of the PDE6 catalytic dimers, PDE6AB heterodimer in rods and PDE6C homodimer in cones, is blocked by two inhibitory γ-subunits (Pγ), allowing for a depolarizing "dark" current through cGMP-gated channels in the plasma membrane. Photoexcitation leads to G protein (transducin)–mediated activation of PDE6 and a drop in cytoplasmic cGMP causing the channels to close and the plasma membrane to hyperpolarize (1). The role of PDE6 in phototransduction is intrinsically linked to its importance to the health and survival of photoreceptor cells. Loss of function of PDE6 leads to elevation of intracellular cGMP and excessive influx of Ca^{2+}, thereby triggering photoreceptor cell death (3–8).

Loss of function of PDE6 can result from mutations in PDE6 causing retinitis pigmentosa, achromatopsia, or cone–rod dystrophy (6, 7, 9–12). Another major reason for PDE6 deficits is malfunction of its specialized retina-specific chaperone AIPL1 (aryl hydrocarbon receptor (AhR)–interacting protein-like 1). AIPL1 was named based on the high sequence identity (49%) and similar domain organization with the ubiquitously expressed AIP (AhR-interacting protein) (13). AIP and AIPL1 both contain an N-terminal FK506-binding protein (FKBP) domain and a C-terminal tetratricopeptide repeat (TPR) domain with three tetratricopeptide repeats. The *AIPL1* gene encoding AIPL1 has been linked to Leber congenital amaurosis, a severe early-onset blindness (13–16). Knockout of AIPL1 in mice revealed selective and drastic destabilization of PDE6, resulting in retinal degeneration (17, 18). This finding suggested that AIPL1 may function as PDE6 chaperone. Such a role of AIPL1 was ultimately established with heterologous expression of active cone PDE6C in the presence of AIPL1 in HEK293 cells (12).

Among the critical interactions that underlie the chaperone activity of AIPL1 is the direct binding of the C-terminal prenyl modifications of the PDE6 catalytic subunits by the AIPL1 FKBP domain (19). The crystal structures of the AIPL1–FKBP with bound farnesyl or geranylgeranyl ligands revealed its unique structural features enabling prenyl moiety binding and unmasked pathogenic mechanisms of the AIPL1 variants in

This work was supported by National Institutes of Health Grant RO1 EY-10843 (to N. O. A.) and Knights Templar Eye Foundation Career Starter Research Grant 18384800 (to R. P. Y). The authors declare that they have no conflicts of interest with the contents of this article. The content is solely the responsibility of the authors and does not necessarily represent the official views of the National Institutes of Health.

This article contains Tables S1 and S2 and Figs. S1–S9.

The atomic coordinates and structure factors (code 6PX0) have been deposited in the Protein Data Bank (http://wwpdb.org/).

[1] To whom correspondence should be addressed: Dept. of Molecular Physiology and Biophysics, 5-532 Bowen Science Bldg., 51 Newton Rd., Iowa City, IA 52242. Tel.: 319-335-7864; Fax: 319-335-7330; E-mail: nikolai-artemyev@uiowa.edu.

[2] The abbreviations used are: PDE, phosphodiesterase; FKBP, FK506-binding protein; PDB, Protein Data Bank; TPR, tetratricopeptide repeat; AhR, aryl hydrocarbon receptor; BLI, biolayer interferometry; SAXS, small-angle X-ray scattering; CSP, chemical shift perturbation; HSQC, heteronuclear single quantum coherence; aa, amino acid(s); DLS, dynamic light scattering; SEC, size-exclusion chromatography; MD, molecular dynamics.

which this binding is deficient (20–22). Known partners of AIPL1 also include HSP90 and the regulatory Pγ subunit of PDE6 (23, 24). Similar to the well-known interactions of TPR domain proteins with HSP90 (25), the AIPL1 TPR domain binds to the C-terminal signature sequence MEVEED of HSP90 (23, 24). AIP utilizes its TPR domain to recruit HSP90 to promote maturation of the AhR (26). The HSP90 chaperone machinery has been implicated in folding of PDE6 (27). Thus, AIPL1 may utilize its FKBP and TPR domains to assemble the chaperone–client complex. However, the role of AIPL1 TPR domain is not limited to generic binding of HSP90. Chimeric protein containing AIPL1–FKBP fused with the AIP–TPR domain failed to chaperone PDE6C in transfected HEK293T cells, suggesting an unique and as-yet-undetermined role of AIPL1–TPR in PDE6 folding (12). Following identification of Pγ as a binding partner of AIPL1 (24), the role of Pγ in PDE6 folding was underscored by the discovery that the AIPL1-dependent expression of functional PDE6 in HEK293T cells is markedly elevated in the presence of Pγ (12).

Despite these findings, the AIPL1–Pγ interface and the mechanism of Pγ as a potent co-chaperone of AIPL1 in folding of PDE6 have not been elucidated. Here, we mapped the sites of the AIPL1 interaction with Pγ using NMR and biolayer interferometry (BLI) approaches, and we demonstrate that the AIPL1 TPR domain binds to the C-terminal region of Pγ. We solved the crystal structure of AIPL1–TPR that was used to generate a model of the AIPL1–TPR complex with Pγ based on the constraints obtained from NMR binding data. Our analysis and the model of the AIPL1–TPR–Pγ complex suggest a specialized adaptation of the TPR domain for chaperoning PDE6. A model of AIPL1 was generated based on the structures of the individual FKBP and TPR domains, the small-angle X-ray scattering (SAXS) profile of AIPL1(1–316), and molecular dynamics simulations. This AIPL1–PDE6 model provides a framework for future structural studies of this critical chaperone–client complex.

Results

AIPL1–TPR domain interacts with the C-terminal region of Pγ, Pγ46–87

Previously we demonstrated that AIPL1 interacts with Pγ, and Pγ acts as a potent co-chaperone of AIPL1 in folding/assembly of PDE6 (12, 24). To identify the interface of this interaction, we utilized an NMR approach by examining chemical shift perturbations (CSPs) of individual ^{15}N-labeled FKBP and TPR domains of AIPL1 in the presence of Pγ fragments (28, 29). The N termini of the Pγ subunits are not conserved among the rod and cone counterparts. Two segments of Pγ, including the central polycationic region Pγ24–45 and the C-terminal region Pγ46–87, have been commonly recognized as functionally important parts of the protein contributing to Pγ interactions with PDE6 catalytic subunits and transducin-α (30–33). We first assessed potential effects of synthetic peptides Pγ24–46 and Pγ46–87 on the ^{15}N/^{1}H HSQC NMR spectra of ^{15}N-AIPL1 FKBP domain (aa 1–161). Neither Pγ24–46 nor Pγ46–87 induced CSPs in the spectrum of ^{15}N-AIPL1–FKBP (Fig. S1). However, Pγ46–87, but not Pγ24–46, caused significant CSPs in backbone amide peaks of the AIPL1–TPR domain (aa 171–316), suggesting that Pγ46–87 binds to the TPR domain (Fig. 1*A* and Fig. S2). Our recently assigned NMR backbone resonances of the AIPL1–TPR domain (29) allowed us to identify the residues on this protein as being a part of the Pγ46–87–binding site as clearly labeled for the significantly perturbed peaks (Fig. 1*A*). In addition, selective and substantial CSPs in the presence of Pγ46–87 were detected in the NMR spectrum of ^{13}C-methyl (IVL)-labeled AIPL1–TPR domain (Fig. 1*B*). Next, we determined whether binding of Pγ46–87 to AIPL1–TPR influences its thermostability using dynamic light scattering (DLS) technique. Pγ46–87 increased the T_{onset} of AIPL1–TPR by ~2 °C (Fig. 2*A*), and it had an even stronger effect (~4–5 °C shift) on the thermostability of the full-length AIPL1 (Fig. 2*B*). Thus, the C-terminal region of Pγ binds to the TPR domain of AIPL1, thereby increasing thermostability of the protein.

Analysis of AIPL1–TPR interaction with the C terminus of Pγ by BLI

The kinetics and affinity of binding for AIPL1–TPR and Pγ46–87 were quantitated using BLI, with N-terminally biotinylated Pγ46–87 attached to a streptavidin biosensor (Fig. 3, *A* and *B*). The association and dissociation kinetics for the interaction were consistent with a 1:1 binding model, with an average association constant (k_a) of 0.8×10^5 M^{-1} s^{-1} and an average dissociation constant (k_d) of 0.38 s^{-1}, yielding a $K_D = k_d/k_a$ of 4.8 μM (Fig. 3*A*). The K_D calculated based on steady-state analysis of the interaction between AIPL1–TPR and Pγ46–87 was comparable (3.0 μM; Fig. 3*B*) and also similar to the K_D value of 2.5 μM previously reported for the binding of the full-length AIPL1 and Pγ (24). This confirms that the interface is largely confined to the TPR domain and the C-terminal 46–87 residues of Pγ. Interestingly, the highly homologous TPR domain of AIP failed to appreciably bind to Pγ46–87 in the BLI assay (Fig. S3), highlighting the specificity of AIPL1–TPR–Pγ interaction. To narrow down the Pγ C-terminal site for binding to AIPL1–TPR, we conducted the BLI assay using N-terminally biotinylated Pγ63–87. The association data for up to 15 μM of AIPL1–TPR were fitting well to a 1:1 binding model with the average k_a of $1.6 \pm 0.2 \times 10^5$ M^{-1} s^{-1} (Fig. 3*C*). A K_D of 3.1 μM was estimated from the kinetics data using the average k_d of 0.49 ± 0.02 s^{-1} from the dissociation phase of the assay, whereas a K_D of 4.6 μM was derived from the steady-state analysis (Fig. 3*D*). These results indicate that the 25 C-terminal residues of Pγ encompass most if not all of the contacts with AIPL1–TPR.

Mapping the interface between the Pγ C terminus and AIPL1–TPR by NMR

To determine the minimal region of the C-terminal fragment of Pγ required for binding to AIPL1–TPR, as well as how various Pγ peptides perturb the residues or binding site(s) on AIPL1–TPR, we performed further NMR binding experiments by titrating Pγ C-terminal fragments with different lengths including Pγ63–87, Pγ70–87, Pγ74–87, and Pγ63–83 into AIPL1–TPR. Clearly, Pγ63–87 binds to AIPL1–TPR as shown by both ^{15}N and ^{13}C HSQC spectra (Fig. 4), and Pγ63–87 bind-

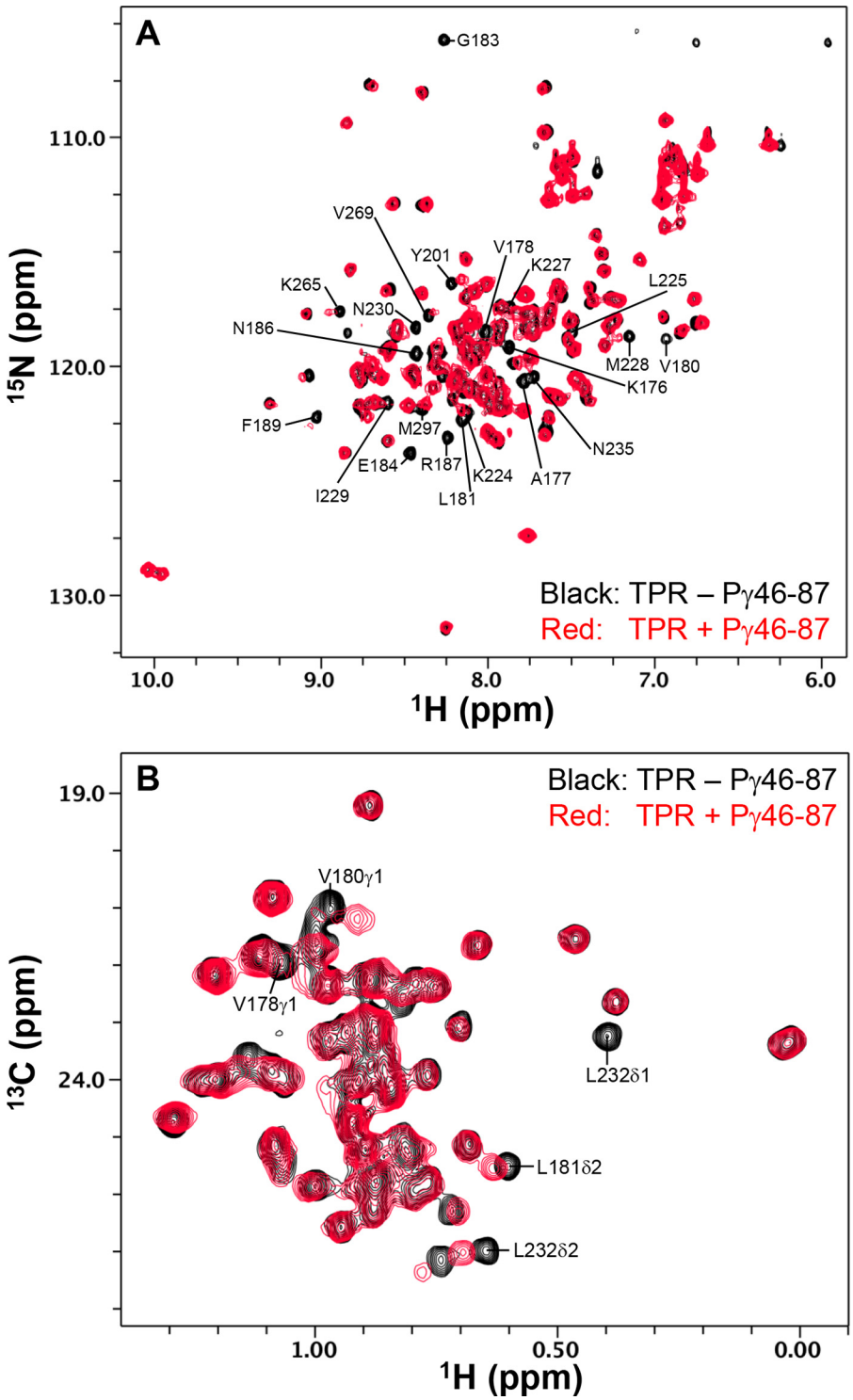

Figure 1. NMR spectra of human uniformly ^{15}N- and ^{13}C-methyl (IVL)–labeled AIPL1 TPR domain acquired in the presence and absence of Pγ46–87. *A*, overlay of ^{15}N/^{1}H HSQC spectra. *B*, overlay of ^{13}C/^{1}H HSQC spectra. The significantly perturbed backbone amide and methyl peaks upon Pγ peptide binding are labeled using the WT protein sequence numbering. In these experiments, the TPR and Pγ peptide concentrations used were 157 and 166 μM, respectively.

ing perturbs the same set of residues on AIPL1–TPR to a similar degree as observed for Pγ46–87 binding (Figs. 1 and 4). This result indicates that Pγ46–87 and Pγ63–87 binds to the same site on AIPL1–TPR, and Pγ residues 46–62 are not required for binding to AIPL1–TPR. This result is also consistent with the similar binding affinity detected by BLI for Pγ46–87 and Pγ63–87.

NMR titration of Pγ70–87 showed that Pγ70–87 binds to the same site on AIPL1–TPR as Pγ63–87 or Pγ46–87 because the same set of residues on AIPL1–TPR are affected upon adding Pγ70–87 (Fig. S4). However, higher Pγ70–87 concentration (Pγ:AIPL1–TPR ratio, 1.6:1) is needed to detect a similar degree of perturbations of these affected residues. During the titration experiments, we noted that Pγ70–87 slowly forms a

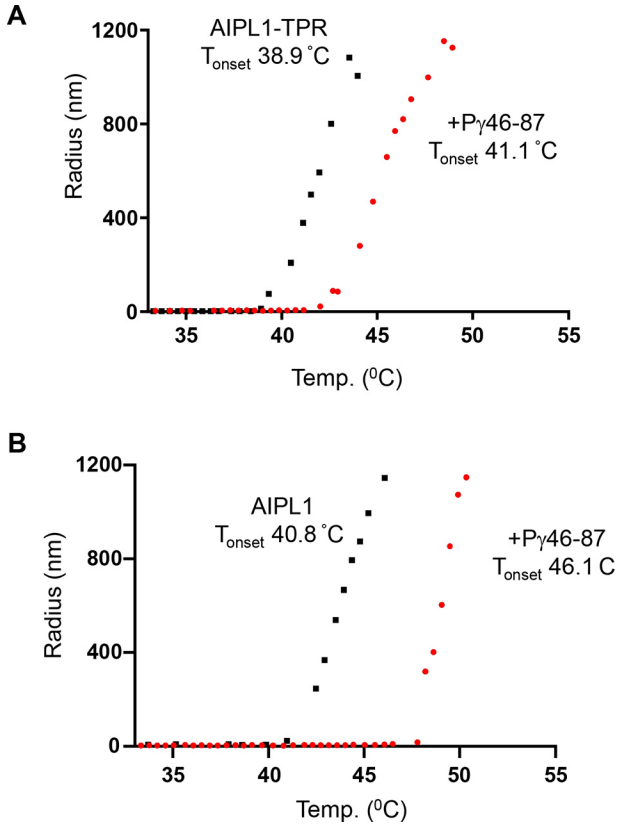

Figure 2. Thermal denaturation, as determined by DLS, for 165 μM AIPL1–TPR (*A*) and for 135 μM AIPL1(1–316) (*B*) in the absence (*squares*) or presence of 330 μM of Pγ46–87 (*circles*). Representative experiments are shown. For experiments performed in triplicate, $T_{m\text{-}onset}$ (°C) values are: AIPL1–TPR, 39.0 ± 0.4; AIPL1–TPR + Pγ46–87, 41.7 ± 0.3; AIPL1(1–316), 41.0 ± 0.3; and AIPL1(1–316) + Pγ46–87, 45.4 ± 0.2 (means ± S.E.). *Temp.*, temperature.

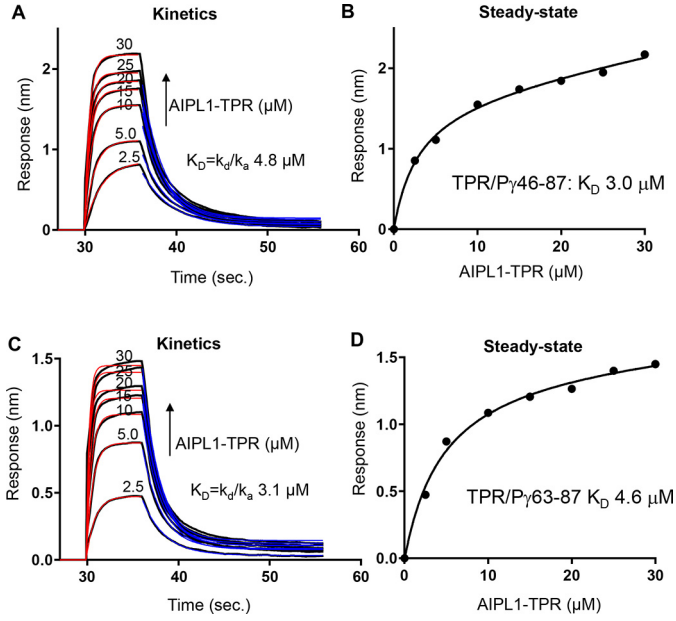

Figure 3. *A*, kinetics of association and dissociation for AIPL1–TPR and biotinylated Pγ46–87 coupled to a streptavidin biosensor as determined using BLI. Representative curves are shown. The processed data curves are *black*, and the nonlinear regression fits from the 1:1 binding model are *red* (association; $k_{on} = 0.8 \pm 0.1 \times 10^5\ M^{-1}\ s^{-1}$) and *blue* (dissociation; $k_d = 0.38 \pm 0.02\ s^{-1}$) (means ± S.E.). *B*, the steady-state binding curve obtained from data in *A*; $K_D = 3.0\ \mu M$. For $n = 5$ experiments, $K_D = 4.1 \pm 1.4\ \mu M$ (means ± S.E.). *C*, kinetics of association and dissociation for AIPL1–TPR and biotinylated Pγ63–87 coupled to a streptavidin biosensor as determined using BLI. Representative curves are shown (*black*). The nonlinear regression fits from the 1:1 binding model are *red* (association; $k_{on} = 1.6 \pm 0.1 \times 10^5\ M^{-1}\ s^{-1}$) and *blue* (dissociation; $k_d = 0.49 \pm 0.02\ s^{-1}$) (means ± S.E.). *D*, the steady-state binding curve obtained from data in *C*; $K_D = 4.6\ \mu M$. For $n = 6$ experiments, $K_D = 5.0 \pm 0.6\ \mu M$ (means ± S.E.).

gel-like solution, indicating reduced solubility. This may have affected the quantification of the peptide and be responsible for the increase in peptide concentration needed to see the similar effect.

NMR titration of Pγ74–87 showed that this peptide binds to AIPL1–TPR very weakly and caused very small CSPs of AIPL1–TPR even at the higher Pγ:AIPL1–TPR ratio of 4.8:1 (762 μM Pγ74–87 and 160 μM AIPL1–TPR). A comparison of Pγ70–87 and Pγ74–87 binding to AIPL1–TPR suggests that Pγ residues 70–73 are required for the interaction.

NMR titration of Pγ63–83 revealed that this peptide binds to AIPL1–TPR because significant CSPs are observed in both ^{15}N and ^{13}C HSQC spectra (Fig. S5), but this peptide binds to AIPL1–TPR weaker than Pγ63–87 because higher Pγ63–83 concentration is needed to induce similar degrees of CSPs (Fig. 4 and Fig. S5). Interestingly, comparing the shift perturbations caused by the binding Pγ63–87 (Fig. 4) and Pγ63–83 (Fig. S5), it is clear that the residues located near the N-terminal of AIPL1–TPR including the backbone amides of Ala-177, Gly-183, Glu-184, Asn-186, and Arg-187 (Fig. S5*A*) and the side chains of Val-178γ1, Val-180γ1, and Leu-232δ1 (Fig. S5*B*) are much less affected by the binding of Pγ63–83. These results indicate that Pγ C-terminal residues 84–87 bind near these residues. Thus, these NMR titration experiments established that Pγ70–87 is the required minimal sequence for binding to AIPL1–TPR. Furthermore, our NMR results implicate two short stretches of Pγ, Pγ70–73 and Pγ84–87, as being critical in Pγ binding to AIPL1–TPR.

Crystal structure of AIPL1–TPR

Given the unique and critical role of the AIPL1 TPR domain in chaperoning PDE6, we sought to solve its crystal structure. The use of His_6-tagged AIPL1(171–316) led to well-diffracting crystals. All residues of AIPL1–TPR, except for the N-terminal nine residues and the C-terminal two residues were well-resolved in electron density (Table S1) (PDB code 6PX0). The crystal structure revealed a typical TPR domain fold with three TPR repeats (Fig. 5*A*). TPR1, TPR2, and TPR3 are comprised of antiparallel α-helices 1–2, 3–4, and 5–6, respectively, followed by α-helix 7. A regular repeat of α-helices generates a right-handed helical array and creates a groove that often serves as a binding surface for binding partners of TPR domain proteins (Fig. 5*B*). AIPL1–TPR is structurally very similar to the TPR domain of AIP, and these two structures are superimposable with a root-mean-square deviation of 1.2 Å for 128 Cα atoms (Fig. 5*B*) (34). In contrast to the AIP–TPR structure, electron density for the nine N-terminal residues of AIPL1–TPR preceding helix α1 is missing. However, the N-terminal helix of AIPL1–TPR may have been affected by the crystal packing. Furthermore, the NMR analysis indicated that residues 176–190 form an α-helix in solution (29). Thus, the N-terminal helix of AIPL1–TPR is longer than it is observed in the structure. One

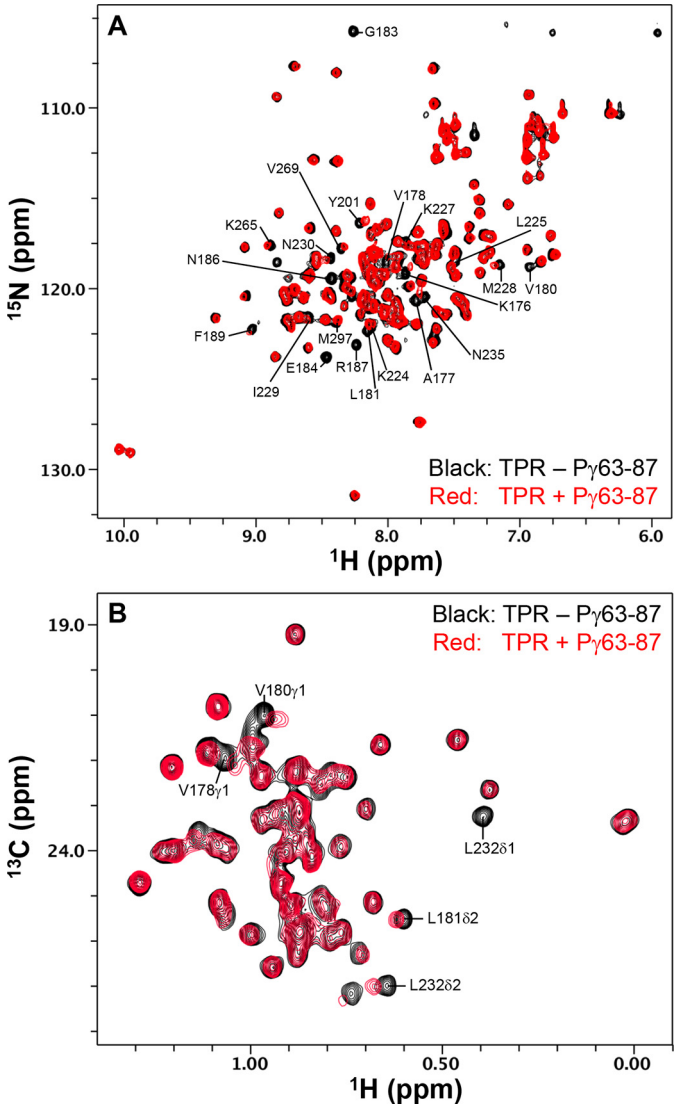

Figure 4. NMR spectra of human uniformly ^{15}N- and ^{13}C-methyl (IVL)–labeled AIPL1 TPR domain acquired in the presence and absence of Pγ63–87. *A*, overlay of ^{15}N/^{1}H HSQC spectra. *B*, overlay of ^{13}C/^{1}H HSQC spectra. The significantly perturbed backbone amide and methyl peaks upon Pγ peptide binding are labeled using the WT protein sequence numbering. In these experiments, the used TPR and Pγ peptide concentrations were 157 and 163 μM, respectively.

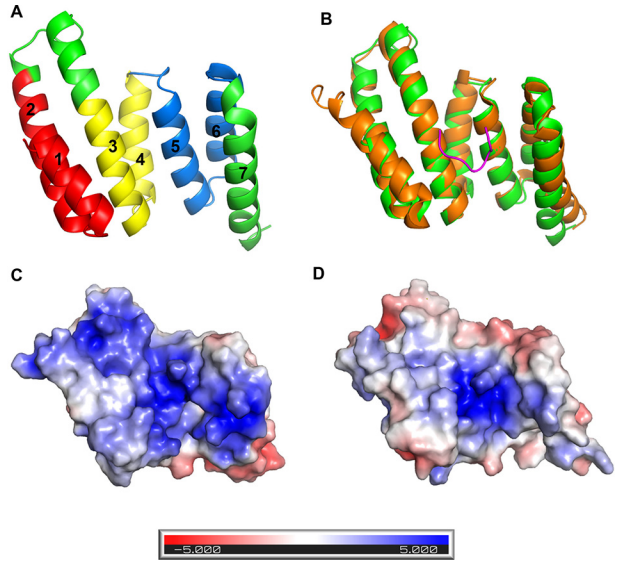

Figure 5. *A*, crystal structure of the human AIPL1 TPR domain. Residues AIPL1(180–314) are resolved in electron density. TPR repeats I (helices α1 and α2), II (helices α3 and α4), and III (helices α5 and α6) are shown in *red*, *yellow*, and *blue*, respectively. *B*, overlay of the structures of AIPL1–TPR (*green*) and AIP–TPR (*orange*) complexed with the HSP90 C terminus, SRMEEVD (*magenta*) (PDB code 4AIF). *C* and *D*, electrostatic surface representations (units K_bT/e_c) of AIPL1–TPR (*C*) and AIP–TPR (*D*). The *color scale* shows electrostatic potential: *red* indicates negative, and *blue* indicates positive.

interesting difference between the structures of the TPR domains of AIPL1 and AIP appears to be a surface charge distribution on the ligand-binding groove of the proteins. The overall surface is positively charged in both TPR domains, but in AIPL1–TPR the positive charge is more dispersed compared with a relatively focal positive pocket in AIP–TPR (Fig. 5, *C* and *D*).

Modeling the complex of AIPL1–TPR with Pγ63–87

Pγ63–87 contains two short α-helices composed of residues 69–74 (α1) and 78–84 (α2), as shown by the crystal structure of Pγ46–87 in complex with G-protein transducin-α and RGS9 (PDB code 1FQJ) (33). These helices match well with the helical propensities of the full-length Pγ alone determined earlier by NMR (35). Therefore, we have docked Pγ63–87 into the crystal structure of AIPL1–TPR with the CNS program (36) by using the NMR restraints derived from the surface-exposed and chemical shift–perturbed residues of AIPL1–TPR upon binding of Pγ63–87 as revealed from the NMR binding experiments. During docking, the Pγ α1 and α2 secondary structures are maintained, but the relative orientation of these two α-helices as well as the Pγ loops are kept fully flexible. Moreover, the α2 helix and the C-terminal four residues of Pγ are kept parallel to the N-terminal α1 and α3 helices of AIPL1–TPR because this binding mode is most consistent with the NMR binding data where deletion of the C-terminal four residues of Pγ significantly reduced CSPs of the residues localized to the N-terminal α1 and α3 helices of AIPL1–TPR (Fig. S5). The docked and energy-minimized model of AIPL1–TPR in complex with Pγ63–87 is shown in Fig. 6 where the significantly perturbed and most severely perturbed residues of AIPL1–TPR upon binding to Pγ63–87 are colored in *red* and *magenta*, respectively.

In this model, the Pγ C-terminal α2 helix is oriented parallel to AIPL1–TPR N-terminal α1, predominantly via hydrophobic interaction through the Pγ residues (Leu-78 and Leu-81) and the AIPL1–TPR residues (Phe-189, Tyr-201, and Leu-232). The Pγ C-terminal hydrophobic residues Ile-86–Ile-87 interact with the AIPL1–TPR hydrophobic patch consisting of Leu-208, Leu-211, and Leu-225. The hydrophobic residues Trp-70 and Phe-73 of Pγ C-terminal α1 helix interact with the AIPL1–TPR hydrophobic residues Tyr-268, Val-269, and Val-290, whereas the hydrophilic residues Glu-71 and Asn-74 of Pγ α1 helix interact with AIPL1–TPR Arg-303 and Arg-272. Interestingly, the conformation of Pγ63–87 modeled in our complex (Fig. 6) is similar to the conformations of the Pγ C terminus observed in the crystal structure of the PDE5/6 catalytic domain in complex with Pγ70–87 (32), and in the recent cryo-EM structure of PDE6/Pγ complex (37). In these structures, the Pγ C-terminal

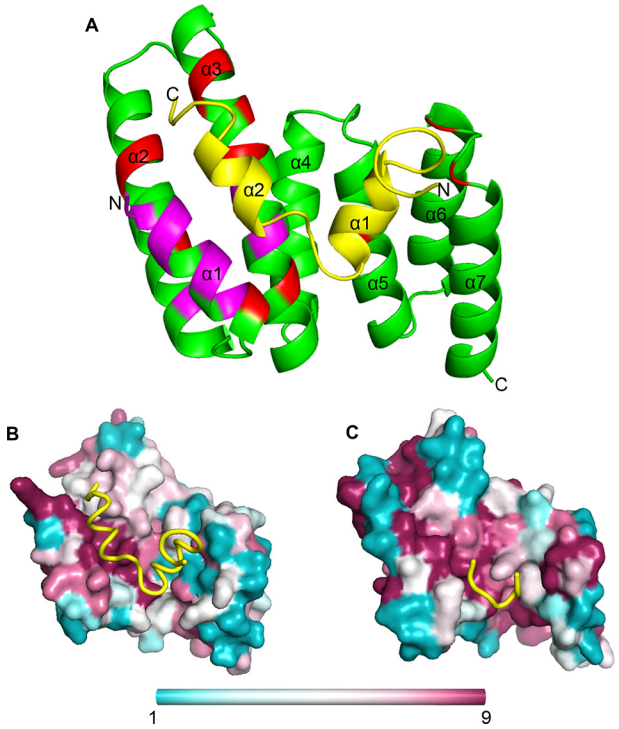

Figure 6. *A*, structural model of the human AIPL1 TPR domain in complex with Pγ63–87. The Pγ63–87 peptide was docked into the crystal structure (aa 180–314) of human AIPL1 TPR domain using the NMR restraints obtained from the analysis of Pγ peptide binding to the protein. The Pγ α1 and α2 secondary helix structures were derived from the PDB structure (PDB code 1FQJ). The Pγ peptide is shown in *yellow*. The *red* and *magenta* ribbons indicate the TPR residues that were significantly perturbed (with $\Delta\delta_{ppm} \geq 0.053$ ppm) and most severely perturbed (with $\Delta\delta_{ppm} \geq 0.10$ ppm) by the binding of the Pγ peptide, respectively. *B* and *C*, surface representations for AIPL1–TPR (*B*) and AIP–TPR (*C*) colored by residue conservations scores derived from ConSurf analysis of a sample of 87 AIPL1–TPR orthologs (*B*) and 89 AIP–TPR orthologs (*C*). The sequences for the analysis with maximal identity of 97% and minimal identity of 60% were collected from the UniProt database. The color scale is as follows: 9, *magenta*, conserved; and 1, *cyan*, variable. Pγ63–87 (*B*) and the C terminus of HSP90 (*C*) are shown as *yellow tubes*.

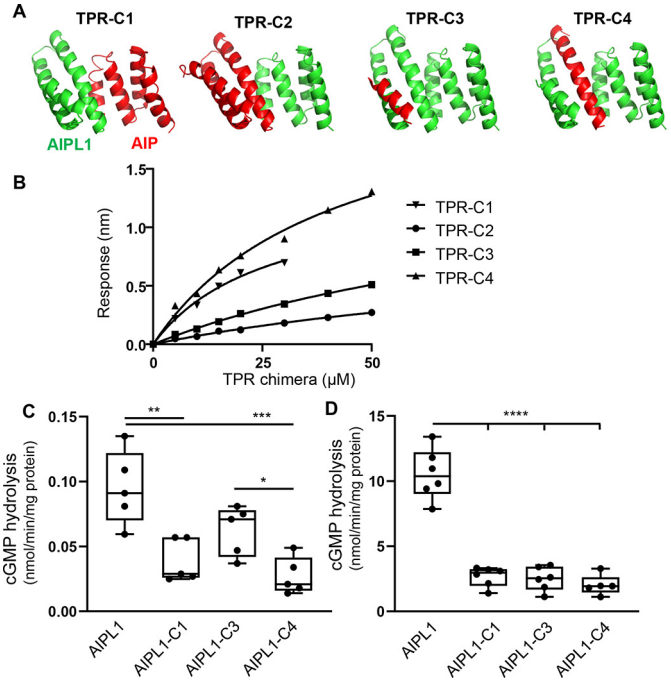

Figure 7. *A*, cartoon representations of AIPL1–AIP TPR chimeras. *B*, steady-state binding curves for AIPL1–TPR chimeras and biotinylated Pγ63–87 coupled to a streptavidin biosensor as determined using BLI. For the shown representative curves, the K_d (μM) values are: TPR-C1, 28; TPR-C2, 118; TPR-C3, 104; and TPR-C4, 41. For experiments performed in triplicate, the K_d (μM) values are: TPR-C1, 33 ± 3; TPR-C2, 110 ± 20; TPR-C3, 125 ± 15; and TPR-C4, 43 ± 1 (means ± S.E.). *C*, cGMP hydrolysis in extracts of HEK293T cells co-transfected with PDE6C, AIPL1 or AIPL1–AIP chimeras. *D*, cGMP hydrolysis in extracts of HEK293T cells transfected as in *C* except with addition of the Pγ vector (untransfected control is subtracted). Because Pγ is the inhibitory subunit of PDE6, the samples with co-expression of Pγ were treated with trypsin to selectively remove Pγ before conducting the assay. The data were analyzed by one-way analysis of variance with Tukey's multiple comparisons follow-up test. Whiskers represent minimum and maximum. *Boxes* represent interquartile range. The *line* represents the median, and *dots* represent data points. The average PDE activity values (nmol min^{-1} mg^{-1}) in *C* and *D* are: AIPL1, 0.10 ± 0.01 and 10.5 ± 0.8; AIPL1-C1, 0.04 ± 0.01 and 2.7 ± 0.3; AIPL1-C3, 0.06 ± 0.01 and 2.4 ± 0.4; and AIPL1-C4, 0.03 ± 0.01 and 2.1 ± 0.3 (means ± S.E., $n \geq 5$).

α2 helix is also present, and the bending angle between the Pγ C-terminal α1 and α2 helical segments is similar to that in our model. However, instead of an α2 helix as modeled, residues 69–74 in the PDE/Pγ structures assume a coil-like conformation. This is not surprising because this helix is very short and furthermore contains a Pro at the N-terminal side (Pro-69).

AIPL1–TPR has been previously shown to bind the C terminus of HSP90 (23). The model of the complex of AIPL1–TPR with Pγ63–87 indicated overlapping Pγ– and HSP90-binding sites (Figs. 5*B* and 6*A*). We confirmed this by comparing the patterns of the CSPs of the perturbed residues upon binding the C-terminal HSP peptide (TSRMEEVD) and Pγ63–87 to AIPL1–TPR (Fig. S6 and Fig. 4)

Probing the AIPL1–TPR–Pγ63–87 interface with chimeric AIPL1–AIP proteins

To identify residues of AIPL1–TPR that are likely to contribute to binding of Pγ63–87, we first conducted conservation analysis of its ligand binding surface using ConSurf (38). This analysis revealed that our model of the complex placed Pγ63–87, in particularly its α2 and the C terminus, over a highly conserved patch of AIPL1–TPR (Fig. 6*B*). Moreover, many of the TPR residues with largest CSPs caused by binding of Pγ63–87 are highly conserved. However, nearly all of these residues were not AIPL1-specific but were identical or homologous to residues at equivalent positions in AIP. Furthermore, the conservation analysis of the ligand-binding surface of AIP–TPR revealed a pattern of conservation similar to that in AIPL1–TPR (Fig. 6, *B* and *C*). Thus, the selectivity of AIPL1 for Pγ63–87 is likely defined by the overall conformation of the binding surface with contribution from multiple rather than few residues. Therefore, we utilized a chimera AIPL1–AIP TPR approach to test the significance of various segments of AIPL1–TPR for the interaction with Pγ63–87 and for the chaperone activity of AIPL1. Initially, two chimeric TPR domains, TPR-C1 and TPR-C2, were constructed as shown in Fig. 7*A*, and examined for thermostability and the ability to bind Pγ63–87 (Table S2 and Fig. 7*B*). Both chimeras were thermally stable, indicating proper overall folding. Chimera TPR-C1 containing α1–α3 α-helices of AIPL1–TPR and α4–α7 of AIP–TPR retained higher affinity for Pγ63–87 compared with the reciprocal chimera TPR-C2 (Fig. 7*B* and Table S2). To test the ability of the C1 and C2 TPR domains to support the chaperone activity of AIPL1,

the full-length AIPL1 proteins (AIPL1-C1 and AIPL1-C2) with the corresponding chimeric TPR domains have been generated for co-expression with PDE6C in the absence or presence of Pγ in HEK293T cell (Fig. 7). AIPL1-C1 induced ~40% of basal PDE6C activity observed with the WT AIPL1 (Fig. 7*C*) and ~27% of PDE6C activity compared with WT AIPL1 when the co-expression system included Pγ (Fig. 7*D*). Accordingly, in the presence of Pγ, folding of PDE6C was increased ~105-fold by AIPL1, and ~67-fold by AIPL1-C1 (Fig. 7, *C* and *D*). Thus, the reduction in affinity for Pγ in TPR-C1 was accompanied by the reduction in the Pγ potentiation of the chaperone activity of AIPL1-C1. In contrast, AIPL1-C2 failed to chaperone PDE6C regardless of the presence of Pγ. In agreement with NMR data and the model, the results with TPR-C1, TPR-C2, and AIPL1-C1 and AIPL1-C2 are consistent with the α1 and α3 being the most critical Pγ binding and chaperone activity determinants. TPR-C3 and TPR-C4 were constructed to further probe the role of α1 and α3, respectively (Table S2 and Fig. 7*A*). TPR-C3 was significantly more impaired in Pγ63–87 binding than TPR-C4 (Fig. 7*B*). However, the basal chaperone activity of AIPL1-C3 was ~60% of that for WT AIPL1, which was significantly higher than the basal chaperone capacity of AIPL1-C4 (~30%) (Fig. 7*C*). Reflecting a greater decrease in affinity for Pγ63–87 in TPR-C3 compared with TPR-C4, the Pγ potentiation of the chaperone activity of AIPL1-C3 (~40-fold) was weaker than that of AIPL1-C4 (~70-fold) (Fig. 7, *C* and *D*).

Modeling of AIPL1 and its complex with PDE6

A starting model of AIPL1(1–316) was generated using Modeler and the crystal structures of AIPL1–FKBP (PDB code 5U9A), FKBP52 (PDB code 1P5Q), and AIPL1–TPR domain (PDB code 6PX0), which was extended by nine N-terminal residues and two C-terminal residues according to the crystal structure of AIP–TPR (PDB code 4AIF) (20, 34). The model of AIPL1(1–316) thus obtained featured relatively compact conformation with the FKBP domain and the α3 helix of its insert region closely opposing the α1 of the TPR domain (Fig. 8*A*). To probe the fitness of the model, we examined conformation of AIPL1(1–316) in solution by analyzing it with SEC–SAXS. The theoretical SAXS profile for the initial AIPL1(1–316) model fit the experimental SEC–SAXS data with a χ^2 value of 1.67, indicating a general agreement of the model with the protein structure in solution (Fig. 8*D*).

Next, we sampled potential conformations of AIPL1(1–316) that the protein may adopt in complex with PDE6 using molecular dynamics (MD) simulations. In these MD simulations, in addition to the model of apo AIPL1(1–316), we used a complex of AIPL1(1–316) with Pγ63–87 modeled according to the AIPL1–TPR–Pγ63–87 model. Nine 230–280–ns MD simulations of apo AIPL1(1–316) (MD1–MD9) revealed two general types of trajectories. The first trajectory, observed in MD 1, 2, 3, 6, and 8, showed the FKBP domain rotation against the TPR domain with the α3 helix of the insert region moving toward the TPR domain and occupying its ligand-binding surface (Fig. 8*B*). These trajectories produce closed conformation of AIPL1. The second trajectory type featured the movement of insert α3 helix toward the TPR loop α1–α2, where it stayed near the bottom of the TPR domain (MD 4, 5, 7, and 9) (Fig. 8*C*). This is an open

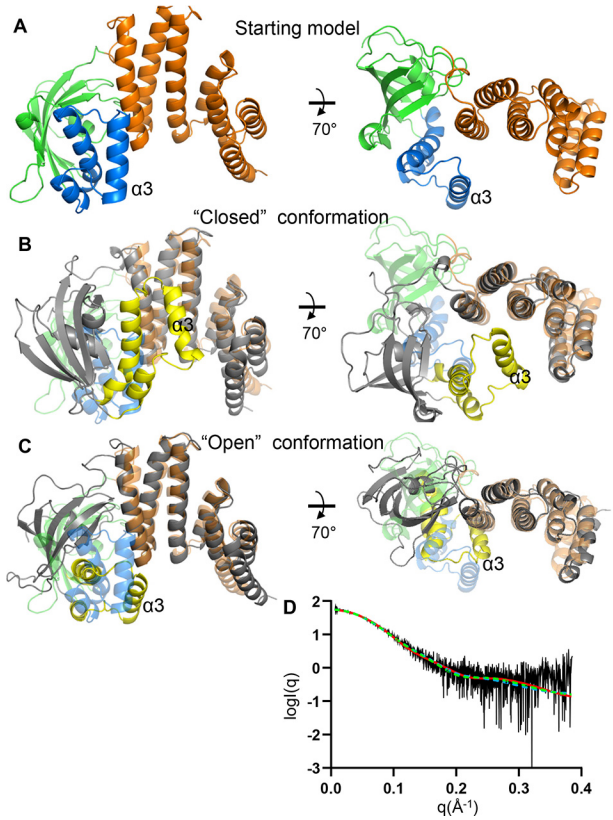

Figure 8. *A*, a starting model of AIPL1(1–316) generated using the structures of AIPL1–FKBP and AIPL1–TPR using Modeler. The FKBP domain of AIPL1 and its insert region are rendered in *green* and *blue*, respectively. The TPR domain is shown in *orange*. *B*, a representative closed conformation of AIPL1(1–316) from MD6 trajectory is shown in *gray* with the insert region shown in *yellow*. Superimposed is the starting model shown in transparent colors as in *A*. TPR α1–α3 were used in superimposition. *C*, a representative open conformation of AIPL1(1–316) from MD5 trajectory is shown as in *B*. *D*, experimental SAXS data for AIPL1(1–316) (*black curve*). The theoretical SAXS profiles calculated for models in *A* (*red curve*), *B* (*green dashed curve*), and *C* (*blue dashed curve*) fit the data with χ^2 values of 1.67, 1.27, and 1.25, respectively.

conformation of AIPL1 that allows unrestricted access to the ligand-binding surface of AIPL1–TPR (Fig. 8*C* and Fig. S7*A*). Theoretical SAXS profiles of all conformations of apo AIPL1(1–316) generated in the MD analysis were compared with the experimental SEC–SAXS data, and the top models from trajectories 5 and 6 featured robust χ^2 values of 1.25 and 1.27, respectively (Fig. 8*D*). Nine 290–400–ns MD simulations of the AIPL1(1–316)/Pγ63–87 complex (MD10-MD18) also revealed two general types of trajectories. One type was similar to the "open conformation" trajectory type of apo AIPL1(1–316) simulations (MD 10,12, 14, 15, and 17) (Figs. S7*B* and S8*A*). No trajectories similar to the "closed conformation" trajectory type of apo AIPL1(1–316) simulations were observed with the complex, apparently because of the occupation of the ligand-binding site by Pγ63–87. Instead, the second alternative type of trajectories involved movement of the insert α3-helix toward the N-end of the TPR α1, *i.e.* in the direction opposite to the open conformation trajectory type of apo AIPL1(1–316) (Figs. S7*B* and S8*B*). To model the complex of AIPL1 with PDE6, we superimposed the AIPL1–TPR–Pγ63–87 model onto the cryo-EM structure of PDE6 (PDB code 6MZB) using the α2 helix of Pγ63–87, which is also an α-helix in the PDE structure

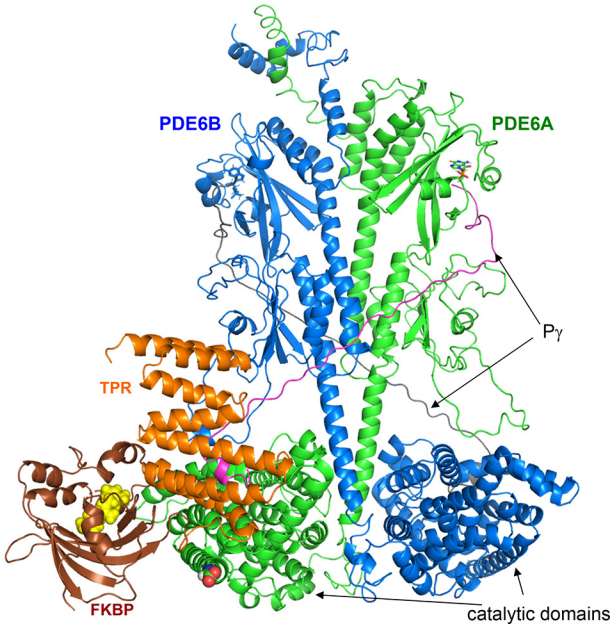

Figure 9. Model of the AIPL1–PDE6 complex. The model was generated by superimposing a representative open conformation of AIPL1(1–316) from MD15 simulation of the AIPL1–Pγ63–87 complex onto the structure of rod PDE6 (PDB code 6MZB). The PDE6A and PDE6B catalytic subunits are shown in *green* and *blue*, respectively. The Pγ subunits are shown in *magenta* and *gray*. The AIPL1 FKBP and TPR domains are rendered in *brown* and *orange*, respectively. The farnesyl moiety is shown as *yellow spheres*, and the C-terminal residue present in PDE6 structure is shown as *spheres* colored by atom type. For clarity, the complex is shown only for the PDEA subunit.

(37). Such superimposition produced no sterical clashes between PDE6 and the AIPL1–TPR domain. Next, we used AIPL1–TPR to superimpose models of AIPL1(1–316) from MD10-MD18 simulations that had better fits (χ^2 values) to the experimental SAXS data. Interestingly, models from the MD trajectories of the open conformation type produced little to no clashes with PDE6, whereas models from MD trajectories of the alternative type severely clashed with the PDE6 catalytic domains. A representative model of the AIPL1–PDE6 complex is shown in Fig. 9. The farnesyl moiety in the FKBP-binding pocket of AIPL1 is in favorable proximity to Gly-822, the last C-terminal residue of PDE6A resolved in the structure, whereas farnesylation occurs at PDE6A–Cys-856. Thus, the model is consistent with simultaneous binding of AIPL1–FKBP to prenylated C termini of PDE6 and AIPL1–TPR to the Pγ C-terminal region.

Role of the insert region α3 helix of AIPL1–FKBP

MD simulations indicated a potentially critical role of the insert region α3 helix in protein dynamics of AIPL1. To probe the significance of this region, we replaced the insert region α3 helix with a small flexible loop comprised of five Gly residues. This mutant AIPL1 protein (AIPL1-Δα3) was thermally stable, and it bound the farnesyl moiety and Pγ46–87 comparably to WT AIPL1 (Fig. S9, *A* and *B*). However, AIPL1-Δα3 completely failed to chaperone PDE6C in the HEK293T system. To determine the molecular mechanism, underlying this failure we conducted MD simulations of the AIPL1-Δα3 model. In three of four simulations, the FKBP and TPR domains completely separated and moved independently of each other (Fig. S9, *C* and *D*). Such separation of the domains would interfere with the ability of AIPL1 to simultaneously bind the prenylated C termini and Pγ subunit of PDE6.

Discussion

The Pγ subunit of PDE6 is essential for the folding and/or assembly of the latter; in the absence of Pγ, virtually no functional PDE6 is formed in mouse photoreceptors, and this leads to rapid retinal degeneration (39). Moreover, in mice bearing a mutation that deletes just two C-terminal Ile residues of Pγ, levels of the catalytic subunits of PDE6 are reduced in the retina (40). Recently, it was discovered that Pγ interacts with AIPL1, an obligate chaperone of PDE6; subsequently, it was hypothesized that this interaction markedly potentiates expression of functional PDE6C in a heterologous system and in photoreceptor cells *in vivo* (12, 24). Our study validates this hypothesis and reveals the molecular underpinning of the important biological effects of Pγ. Specifically, it demonstrates that the main interaction interface between Pγ and AIPL1 is confined to the Pγ C terminus, Pγ63–87, and the TPR domain of AIPL1. Our model of the AIPL1–TPR–Pγ63–87 complex, generated based on the newly solved crystal structure of AIPL1–TPR and on NMR analysis and binding of various Pγ C-terminal peptides to AIPL1–TPR, is supported by our data for the interaction of Pγ63–87 with chimeric AIPL1–AIP TPR domains. In addition, these data established a correlation between the ability of Pγ to elevate expression of functional PDE6C and the affinity of chimeric TPR domains for Pγ63–87. Thus, the biological effects of Pγ as a co-chaperone in folding of PDE6 are mediated by the interaction of Pγ with AIPL1–TPR. Our study also illuminates the puzzling question of why AIPL1 is specific for PDE6. One aspect of the puzzle was that although several essential photoreceptor proteins are prenylated and AIPL1–FKBP appears to bind prenyl moieties irrespective of the sequence of the prenylated peptide or protein (20), only PDE6 is affected significantly in the absence of AIPL1 (17). A second was that although ubiquitous TPR domain proteins, such as AIP, commonly bind HSP90 to assist protein folding, the AIPL1–TPR–HSP90 interaction would not explain the specificity of AIPL1 (25, 41). Our study sheds a new light on the versatility of TPR domains in protein folding by identifying Pγ as a novel TPR protein–binding partner that imparts the selectivity of AIPL1 for its client PDE6.

A model of AIPL1(1–316) based on the crystal structures of AIPL1–TPR, AIPL1–FKBP, and the experimental SAXS profile enabled us to interrogate domain dynamics of the protein. Our findings lend support to the emerging concept of the TPR domain–mediated autoinhibition states of signaling molecules. MD simulations of the AIPL1 model suggested that this protein exists in two main conformations in solution: closed and open. Although the relative orientations of the FKBP and TPR domains differed in these conformations, the domains did not separate in any of the MD simulations of AIPL1(1–316). Another notable feature is that in the closed conformation, the α3-helix of the FKBP insert region occludes the ligand-binding surface of the TPR domain, whereas in the open conformation this surface was freely accessible to binding partners, such as HSP90 and Pγ. Likewise, the prenyl-binding pocket in AIPL1–

FKBP is more accessible in the open conformation. Notably, the closed autoinhibited conformation of AIPL1 is conceptually similar to that of GPSM2-LGN, where the α-helices of GoLoco-GPR motifs occupy the binding surface for TPR domain partners (42). Binding of Gα subunits to GoLoco-GPR releases LGN from autoinhibition and facilitates interaction of the LGN-TPR domain with NuMA (nuclear mitotic apparatus protein), leading to formation of the signaling complex required for asymmetric cell division (42). Another important example of TPR domain–mediated autoinhibition is PP5 (protein phosphatase 5). In this case, the TPR domain engages with and restricts access to the catalytic site (40). This autoinhibition is released by the binding of HSP90 and fatty acids, resulting in the stimulation of phosphatase activity. By analogy to LGN and PP5, the AIPL1 TPR domain partner, HSP90 or Pγ, might shift the equilibrium toward the open conformation, thereby promoting formation of the chaperone–PDE6 complex and enabling the expression of functional PDE6.

Interestingly, when the open conformation of AIPL1 was used in modeling the complex with holoPDE6, few or no clashes of AIPL1 with the PDE6 catalytic subunits were observed. Furthermore, in the resulting models of the AIPL1–PDE6 complex, the prenyl moiety in the FKBP domain binding pocket was in close proximity to the presumed prenylated C-terminal Cys of the PDE6 catalytic subunit. Thus, our models of the AIPL1–PDE6 complex are consistent with simultaneous binding of the prenylated C termini of the PDE6 catalytic subunits and Pγ subunits to the AIPL1 FKBP and TPR domains, respectively. The MD simulations suggested that the α3-helix of the FKBP insert region plays an important role in the dynamics and interdomain interactions of AIPL1 and demonstrated that deletion of this region (AIPL1-$\Delta\alpha$3) leads to physical separation of the FKBP and TPR domains. The finding that AIPL1-$\Delta\alpha$3 fully retained its capacity for binding of the prenyl moieties and Pγ46–87 yet lost the ability to chaperone PDE6 shows that specific orientations of AIPL1 domains are required for it to simultaneously bind the two ligands.

Our data suggest that the HSP90 C terminus and Pγ63–87 bind to AIPL1–TPR in a mutually exclusive fashion. We hypothesize the following sequence of interactions during the folding of PDE6. Binding of HSP90 to AIPL1–TPR relieves the autoinhibition in the closed state of AIPL1, facilitating binding of AIPL1–FKBP to the post-translationally prenylated C termini of nascent PDE6 catalytic subunits. Thus, the PDE6 catalytic dimer is recruited to the chaperone complex consisting of AIPL1 and HSP90. In the initial PDE6–AIPL1–HSP90 complex, HSP90 may assist primarily in folding of the PDE6 catalytic domains because functional expression of PDE6 GAF domains in the absence of AIPL1 has been reported (43, 44). During this stage, a small fraction of PDE6 can become catalytically active, and a Pγ-binding site on PDE6 may be partially formed. This model is supported by the basal Pγ-sensitive PDE6 activity resulting from co-expression of the enzyme with AIPL1 in the absence of Pγ (12). During the next step, HSP90 dissociates from PDE6 or is actively outcompeted by Pγ, and Pγ becomes an adaptor between AIPL1–TPR and the PDE6 catalytic domains. In the complex AIPL1–Pγ–PDE6cat (or AIPL1–Pγ–$(PDE6cat)_2$–Pγ–AIPL1, given PDE6 is a catalytic dimer), the affinity of AIPL1 for Pγ–PDE6 is greater than that for PDE6 during the initial stage. This complex may allow AIPL1–TPR to direct the Pγ C terminus to the PDE6 catalytic pocket and/or induce the latter to adopt its native conformation and achieve its full catalytic power.

A sequential model of client protein interaction with ubiquitous, relatively nonselective chaperones such as HSP90 followed by assembly with specialized co-chaperones might be more broadly applicable in the context of protein folding. Future structural studies of the AIPL1–PDE6 complex are expected to reveal mechanistic details of the final steps in PDE6 folding that are critical for visual perception.

Experimental procedures

Plasmids/cloning

DNA sequence encoding human AIPL1–TPR (residues 171–316) was PCR-amplified and cloned as described earlier (29). DNA sequences that encode the full-length human AIP and AIP–TPR (residues 172–317) were PCR-amplified from cDNA isolated from HEK293T cells and cloned into the pET15b vector using NdeI/XhoI and Nco1/Nde1 sites, respectively. Chimeric TPR-C1 in which residues 244–328 of AIPL1 were replaced with residues 245–330 of AIP, was generated in a two-step PCR procedure: (i) a DNA sequence encoding AIP 245–330 was amplified using forward hybrid AIPL1–AIP primers and a reverse primer for AIP with a Nde1 site; and (ii) this PCR product was then used as a reverse primer in a PCR with the AIPL1–TPR template and a forward primer for WT AIPL1–TPR with a NcoI site and His_6 tag. A similar two-step PCR protocol was used to generate TPR-C2, TPR-C3, and TPR-C4 in which residues 162–243, 162–192, and 218–247 of AIPL1 were replaced with residues 163–244, 163–193, and 219–248 of AIP, respectively. The PCR product was then cloned into the pET15b vector using NcoI/NdeI site. The AIPL1-$\Delta\alpha$3 construct was generated by replacing the residues 111–132 of AIPL1 WT with five glycine residues in a two-step PCR procedure. In the first step, the AIPL1(1–110)-Gly-Gly-Gly-Gly-Gly(111–132) sequence was amplified with a forward primer with Nco1 site, His_6 tag and a reverse primer corresponding to AIPL1(100–110)-Gly-Gly-Gly-Gly-Gly(111–132). This PCR product was used as a forward primer in the second PCR amplification with a primer containing the stop codon and Nde1 site. This resulting PCR product was then cloned into the pET15b vector using Nco1/NdeI sites.

The pcDNA3.1 vector for expression of the full-length mouse AIPL1, FLAG tag full-length PDE6, and enhanced GFP–tagged Pγ was described previously (12). Full-length chimeras AIPL1-C1, AIPL1-C2, AIPL1-C3, and AIPL1-C1 in pcDNA3.1 vector were generated similarly to the construction of chimeric TPR domains in pET15b. AIPL1-C1 in which residues 244–328 of AIPL1 were replaced with residues 245–330 of AIP, was generated in a two-step PCR procedure: (i) a DNA sequence encoding AIP 245–330 was amplified using forward hybrid AIPL1–AIP primers and a reverse primer for AIP containing an hemagglutinin tag and XbaI site; and (ii) this PCR product was then used as a reverse primer in a PCR with the AIPL1 template and a forward primer for WT AIPL1 with HindIII site and Kojak

sequence. A similar two-step PCR protocol was used to generate full-length AIPL1-C2, AIPL1-C3, and AIPL1-C4 in which residues 162–243, 162–192, and 218–247 of AIPL1 were replaced with residues 163–244, 163–193, and 219–248 of AIP, respectively. The chimeric constructs were inserted into the HindIII/Xba1 sites of vector pcDNA3.1.

Protein purification

Full-length AIPL1, AIPL1-Δα3, AIPL1–TPR, AIP—TPR, and chimeric TPR-C1, TPR-C2, TPR-C3, and TPR-C4 were expressed in BL21-(DE3) *Escherichia coli* cells and purified over nickel–nitrilotriacetic acid resin (EMD Millipore), followed by ion-exchange chromatography on a HiTrap SP FF (GE Healthcare) as previously described (29). Final purification was achieved by gel-filtration chromatography on a HiLoad 16/600 Superdex 75 column (GE Healthcare) equilibrated against 50 mM Tris·HCl (pH 7.5) buffer containing 250 mM NaCl and 6 mM DTT. Uniformly ^{15}N- and ^{13}C-labeled AIPL1–TPR and uniformly ^{15}N- and selectively ^{13}C-methyl-labeled (for IVL residues) AIPL1–TPR were obtained according to a protocol outlined previously (20, 28, 29). All isotopes were obtained from Sigma–Aldrich.

Dynamic light scattering

DLS was used to examine the degree of polydispersity and thermostability of AIPL1–TPR, AIPL1-Δα3, and TPR chimeras. Purified proteins were concentrated up to 3 mg/ml and used for light-scattering experiments. For Pγ-bound AIPL1–TPR samples Pγ peptide was added in 2.5-fold excess and incubated for 5 h and centrifuged at 45,000 for 1 h. DLS data for thermostability measurements were collected while heating the samples from 20 to 80 °C at 1 °C/min. Onset of protein thermal unfolding ($T_{\text{m-onset}}$) was determined by the sudden increase in hydrodynamic radius during the temperature ramp. Analyses of thermostability of AIPL1, AIPL1–TPR, AIPL1-Δα3 with and without Pγ peptide and TPR chimeras were performed using a DynaPro Nanostar instrument (Wyatt), and the data were analyzed using the Dynamics 7.1.7 software.

Biolayer interferometry binding assay

An Octet RED96 system and streptavidin-coated biosensors (FortéBio, Menlo Park, CA) were used to measure association and dissociation kinetics for Pγ C-terminal peptide (Pγ46–87 and Pγ63–87) with AIPL1, AIPL1-Δα3, AIPL1–TPR domain, TPR-C1, TPR-C2, TPR-C3, and TPR-C4. Binding studies were performed in 20 mM Tris, 250 mM NaCl, 2.5% glycerol, 1 mM tris(2-carboxyethyl)phosphine, 0.5 mg/ml BSA (pH 7.5). All steps were performed at 26 °C, with biosensors stirred into 0.2 ml of sample in each well at 1000 rpm and at a data acquisition rate of 5.0 Hz. N-terminally biotinylated Pγ46–87and Pγ63–87 peptides were loaded onto streptavidin sensors at a concentration of 5 μg/ml for 60–90 s. Data for association and dissociation phases of the assay were collected as shown in Fig. 3 (*A* and *C*). To correct for baseline drift and nonspecific binding, reference sensors with bound Pγ peptide were used in the BLI assays without AIPL1–TPR proteins. Kinetic data fitting was performed using FortéBio Data Analysis software 10.0. For each concentration of AIPL1–TPR, dissociation rate constant (k_d) values were calculated from the corresponding dissociation phases of the curves. These k_d values were used to calculate the association rate constant (k_a) values from the association phases for each concentration according to the equation: $k_a = k_{\text{obs}}\text{-}k_d/[\text{AIPL1}]$. The average k_a and k_d were calculated as means of the individual k_a and k_d values for all curves. K_D was calculated as mean k_d/mean k_a. Steady-state data fitting was performed using the GraphPad Prism 8 software with the equation for one site-specific binding.

Fluorescence binding assays

Labeling of FC (S-farnesyl-L-cysteine) with AMCA (6-((7-amino-4-methylcoumarin-3-acetyl)amino) hexanoic acid, succinimidyl ester) and a FRET assay of assessing the binding of FC–AMCA to AIPL1 and AIPL1-Δα3 were performed using an F-2700 fluorescence spectrophotometer (Hitachi), as described previously (19, 24).

Crystallization and crystal structure determination

Purified AIPL1–TPR was concentrated to 8–12 mg/ml. Crystals of AIPL1–TPR were grown by hanging-drop vapor diffusion at 18 °C, against well buffer containing 100 mM Tris, 5–15% PEG8000 (pH 7.5–8.5) using a TTP LabTech Mosquito crystallization robot (TTP LabTech). The crystals grew over periods of 1–3 weeks. Crystals were cryoprotected using 20% glycerol in mother liquor. Data for the crystals were collected remotely from the University of Iowa Protein Crystallography Facility using the 4.2.2 Beamline at the Advanced Light Source (Berkeley, CA). The crystals were exposed to the beam for 0.1 s at a detector distance of 200 mm with a wavelength of 1 Å at 0.2° oscillation per frame, and data were collected across a 180° rotation. The data sets were indexed and integrated using XDS (45) and scaled using the SCALA (3.3.22) (46). PDB code 4AIF was used as search model, and molecular replacement was done using Phaser (47). Structure was refined using REFMAC (48) and Phenix (49), and manual models were built using Coot (50). All figures of structures and alignments were generated using the PyMOL Molecular Graphics System (version 1.8, Schrödinger, LLC). The atomic coordinates of AIPL1–TPR have been deposited in the Protein Data Bank (PDB code 6PX0).

Small-angle X-ray scattering

SAXS data were collected at the BioCAT (Beamline 18-ID; Advanced Photon Source, Argonne National Laboratory) using an in-line SEC–SAXS configuration (51). Concentrated protein samples of hAIPL1$_{1-316}$ (10 mg/ml) were loaded on a Superdex 75 10/300 GL gel-filtration column (GE Healthcare) equilibrated against gel filtration buffer containing 50 mM Tris, 100 mM NaCl, 2.5% glycerol, and 6 mm DTT. To separate any aggregates or oligomer states, the samples were subjected to scattering analysis in-line with size-exclusion chromatography. Scattering data were collected every 2 s using a 0.5-s exposure on a Pilatus 3 × 1 M pixel detector (DECTRIS) covering a q range of $0.0040 < q < 0.388$ Å^{-1} ($q = 4\pi/\lambda \sin\theta$, where 2θ is the scattering angle). For each protein, the buffer scattering before and after the eluted peak was recorded and used for background correction. The final protein scattering curves were obtained by

scaling the data from the main peak, averaging it and correcting for buffer scattering. BioXTAS RAW and ATSAS 2.8 were used for SAXS data reduction and analysis (52, 53). SAXS data for AIPL1 (1–316) was deposited in the Small Angle Scattering Biological Data Bank (https://www.sasbdb.org)[3] with the accession codes SASDGX4 (https://www.sasbdb.org/data/SASDGX4/dw65ypkmop/)[3] (58).

Cell culture and PDE6 activity assay

HEK293T cells were cultured and maintained in Dulbecco's modified Eagle's medium containing 10% fetal bovine serum (Gibco). The cells were transfected with human PDE6C alone (2 μg) or co-transfected with mouse Pγ, mouse AIPL1 (1 μg each), or both Pγ and AIPL1 (1 μg each) plasmids using FuGENE 6 (Promega) according to the manufacturer's instructions.

For the PDE6C activity assay, PDE6C, AIPL1, or AIPL1 and Pγ co-transfected HEK293T cell lysates were prepared in hypotonic buffer (5 mM Tris-HCl, pH 7.5, 1 mM $MgCl_2$, buffer A) and centrifuged at 125,000 $\times$ *g* for 30 min at 4 °C in a Beckman Optima TLX ultracentrifuge. The supernatants thus obtained were used for all PDE6C activity measurements. cGMP hydrolysis was measured in cell lysates obtained from HEK293T cells 48 h post-transfection. The samples were treated with 0.1 mg/ml tosylphenylalanyl chloromethyl ketone–trypsin (Sigma) on ice for 10 min to selectively degrade Pγ, after which trypsin was inhibited with the addition of 10-fold excess of soybean trypsin inhibitor (Sigma) and incubation for 5 min at 25 °C. Cell lysates (protein concentration, 5–10 mg/ml) were diluted 4–600-fold into 40 μl (final volume) of a buffer containing 20 mM Tris-HCl (pH 7.5), 120 mM NaCl, 2 mM $MgSO_4$, 1 mM 2-mercaptoethanol, 0.1 unit bacterial alkaline phosphatase, 10 μM [^{3}H]cGMP (100,000 cpm) (PerkinElmer Life Sciences) for 15 min at 37 °C. The reaction was stopped by the addition of AG1-X2 cation exchange resin (0.5 ml of 20% bed volume suspension). The samples were incubated for 6 min at 25 °C with occasional mixing and spun at 10,000 $\times$ *g* for 3 min. 0.25 ml of the supernatant was removed for counting in a scintillation counter.

NMR spectroscopy

For the studies of Pγ binding to AIPL1–TPR, NMR spectra were acquired on a Bruker Neo 600-MHz NMR spectrometer equipped with a sensitive QCI-P cryoprobe at 25 °C using uniformly ^{15}N-labeled and selectively ^{13}C-methyl–labeled (for IVL residues) AIPL1–TPR at a protein concentration of ~150 μM in a buffer containing 20 mM sodium phosphate (pH 7.5), 400 mM NaCl, and 6 mM DTT in 90% H_2O, 10% D_2O. For the studies of Pγ binding to AIPL1–FKBP, NMR spectra were acquired on a Bruker Avance II 800 MHz NMR spectrometer equipped with a sensitive TCI cryoprobe at 25 °C using uniformly ^{15}N-labeled and selectively ^{13}C-methyl–labeled (for IVL residues) AIPL1–FKBP or uniformly ^{15}N,^{13}C–labeled AIPL1–FKBP at a protein concentration of ~150 μM in a buffer containing 25 mM sodium phosphate (pH 7.5) and 8 mM DTT in 90% H_2O, 10% D_2O. Pγ binding to AIPL1–TPR or AIPL1–FKBP was analyzed by acquiring ^{15}N/^{1}H and ^{13}C/^{1}H HSQC NMR spectra. The ^{1}H chemical shifts were referenced to 2,2-dimethyl-2-silapentane-5-sulfonate. The collected NMR data were processed using NMRPipe (54) and analyzed using NMRView (55). The model of AIPL1–TPR–Pγ63–87 complex was calculated using the CNS program (36) with the NMR-derived restraints from the analyses of the Pγ binding data.

Modeling and MD simulations

The AIPL1–TPR crystal structure was first extended by nine helical N-terminal residues and two C-terminal residues according to the structure of AIP–TPR (PDB code 4AIF) using YASARA Structure 18.2.7. Extended AIPL1–TPR structure was used together with the structures of AIPL1–FKBP (PDB code 5U9A) and FKBP52 (PDB code 1P5Q:B) as input into Modeler (56) to produce the initial model of AIPL1(1–316).

MD simulations were performed using YASARA Structure 18.2.7 and the md_runfast macro. The simulations were run using the AMBER14 force field in water at a temperature of 298 K, pH of 7.4, and NaCl concentration of 0.9%. The particle mesh Ewald summation was used to compute long-range coulombic interactions with a periodic cell boundary and a cutoff of 8 Å. The MD simulations were analyzed using the md_analyze macro in YASARA and PyMOL programs. The Crysol program (57) was used to generate and compare fits of theoretical SAXS profiles of the models from MD trajectories (4 models per 1 ns of MD simulation) to experimental SAXS data (χ^2 values). Models of AIPL1(1–316) from MD simulations with low χ^2 values were superimposed with the model of the AIPL1–TPR–Pγ63–87 complex and subsequently overlaid with the structure of PDE6 (PDB code 6MZB) by aligning the α2-helix residues of Pγ, Pγ78–83.

Author contributions—R. P. Y., L. Y., and N. O. A. data curation; R. P. Y., L. Y., and N. O. A. formal analysis; R. P. Y., K. B., L. Y., and N. O. A. investigation; R. P. Y., L. Y., and N. O. A. methodology; N. O. A. conceptualization; N. O. A. funding acquisition; N. O. A. project administration.

Acknowledgments—We thank Jay Nix (Molecular Biology Consortium 4.2.2 Beamline, Advanced Light Source) for aid in remote data collection, Lokesh Gakhar for help with X-ray data analysis, Srinivas Chakravarty (BioCAT Facility, Advanced Photon Source) for help in SAXS data collection, and Nicholas Schnicker (Protein and Crystallography Facility, University of Iowa) for assistance with BLI data collection. This research used resources of the Advanced Light Source, a Department of Energy Office of Science user facility under Contract DEAC02-05CH11231 and resources of the Advanced Photon Source, a U.S. Department of Energy Office of Science User Facility operated for the Department of Energy Office of Science by Argonne National Laboratory under Contract DE-AC02-06CH11357 and supported by Grant 9 P41 GM103622 from NIGMS, National Institutes of Health. Use of the Pilatus 3 $\times$ 1M detector was provided by Grant 1S10OD018090-01 from NIGMS, National Institutes of Health. We also acknowledge use of resources at the Carver College of Medicine's Protein and Crystallography Facility at the University of Iowa.

[3] Please note that the JBC is not responsible for the long-term archiving and maintenance of this site or any other third party hosted site.

References

1. Arshavsky, V. Y., and Burns, M. E. (2014) Current understanding of signal amplification in phototransduction. *Cell. Logist.* **4,** e29390 CrossRef Medline
2. Cote, R. H. (2004) Characteristics of photoreceptor PDE (PDE6): similarities and differences to PDE5. *Int. J. Impot. Res.* **16,** S28–S33 CrossRef Medline
3. Farber, D. B., and Lolley, R. N. (1974) Cyclic guanosine monophosphate: elevation in degenerating photoreceptor cells of the C3H mouse retina. *Science* **186,** 449–451 CrossRef Medline
4. Bowes, C., Li, T., Danciger, M., Baxter, L. C., Applebury, M. L., and Farber, D. B. (1990) Retinal degeneration in the rd mouse is caused by a defect in the β subunit of rod cGMP-phosphodiesterase. *Nature* **347,** 677–680 CrossRef Medline
5. Pittler, S. J., and Baehr, W. (1991) Identification of a nonsense mutation in the rod photoreceptor cGMP phosphodiesterase β-subunit gene of the rd mouse. *Proc. Natl. Acad. Sci. U.S.A.* **88,** 8322–8326 CrossRef Medline
6. McLaughlin, M. E., Ehrhart, T. L., Berson, E. L., and Dryja, T. P. (1995) Mutation spectrum of the gene encoding the β subunit of rod phosphodiesterase among patients with autosomal recessive retinitis pigmentosa. *Proc. Natl. Acad. Sci. U.S.A.* **92,** 3249–3253 CrossRef Medline
7. Dryja, T. P., Rucinski, D. E., Chen, S. H., and Berson, E. L. (1999) Frequency of mutations in the gene encoding the α subunit of rod cGMP-phosphodiesterase in autosomal recessive retinitis pigmentosa. *Invest. Ophthalmol. Vis. Sci.* **40,** 1859–1865 Medline
8. Wang, T., Tsang, S. H., and Chen, J. (2017) Two pathways of rod photoreceptor cell death induced by elevated cGMP. *Hum. Mol. Genet.* **26,** 2299–2306 CrossRef Medline
9. Chang, B., Grau, T., Dangel, S., Hurd, R., Jurklies, B., Sener, E. C., Andreasson, S., Dollfus, H., Baumann, B., Bolz, S., Artemyev, N., Kohl, S., Heckenlively, J., and Wissinger, B. (2009) A homologous genetic basis of the murine cpfl1 mutant and human achromatopsia linked to mutations in the PDE6C gene. *Proc. Natl. Acad. Sci. U.S.A.* **106,** 19581–19586 CrossRef Medline
10. Thiadens, A. A., den Hollander, A. I., Roosing, S., Nabuurs, S. B., Zekveld-Vroon, R. C., Collin, R. W., De Baere, E., Koenekoop, R. K., van Schooneveld, M. J., Strom, T. M., van Lith-Verhoeven, J. J., Lotery, A. J., van Moll-Ramirez, N., Leroy, B. P., van den Born, L. I., *et al.* (2009) Homozygosity mapping reveals PDE6C mutations in patients with early-onset cone photoreceptor disorders. *Am. J. Hum. Genet.* **85,** 240–247 CrossRef Medline
11. Grau, T., Artemyev, N. O., Rosenberg, T., Dollfus, H., Haugen, O. H., Cumhur Sener, E., Jurklies, B., Andreasson, S., Kernstock, C., Larsen, M., Zrenner, E., Wissinger, B., and Kohl, S. (2011) Decreased catalytic activity and altered activation properties of PDE6C mutants associated with autosomal recessive achromatopsia. *Hum. Mol. Genet.* **20,** 719–730 CrossRef Medline
12. Gopalakrishna, K. N., Boyd, K., Yadav, R. P., and Artemyev, N. O. (2016) Aryl hydrocarbon receptor-interacting protein-like 1 is an obligate chaperone of phosphodiesterase 6 and is assisted by the γ-subunit of its client. *J. Biol. Chem.* **291,** 16282–16291 CrossRef Medline
13. Sohocki, M. M., Bowne, S. J., Sullivan, L. S., Blackshaw, S., Cepko, C. L., Payne, A. M., Bhattacharya, S. S., Khaliq, S., Qasim Mehdi, S., Birch, D. G., Harrison, W. R., Elder, F. F., Heckenlively, J. R., and Daiger, S. P. (2000) Mutations in a new photoreceptor-pineal gene on 17p cause Leber congenital amaurosis. *Nat. Genet.* **24,** 79–83 CrossRef Medline
14. Sohocki, M. M., Perrault, I., Leroy, B. P., Payne, A. M., Dharmaraj, S., Bhattacharya, S. S., Kaplan, J., Maumenee, I. H., Koenekoop, R., Meire, F. M., Birch, D. G., Heckenlively, J. R., and Daiger, S. P. (2000) Prevalence of AIPL1 mutations in inherited retinal degenerative disease. *Mol. Genet. Metab.* **70,** 142–150 CrossRef Medline
15. Dharmaraj, S., Leroy, B. P., Sohocki, M. M., Koenekoop, R. K., Perrault, I., Anwar, K., Khaliq, S., Devi, R. S., Birch, D. G., De Pool, E., Izquierdo, N., Van Maldergem, L., Ismail, M., Payne, A. M., Holder, G. E., *et al.* (2004) The phenotype of Leber congenital amaurosis in patients with AIPL1 mutations. *Arch. Ophthalmol.* **122,** 1029–1037 CrossRef Medline
16. Koenekoop, R. K. (2004) An overview of Leber congenital amaurosis: a model to understand human retinal development. *Surv. Ophthalmol.* **49,** 379–398 CrossRef Medline
17. Ramamurthy, V., Niemi, G. A., Reh, T. A., and Hurley, J. B. (2004) Leber congenital amaurosis linked to AIPL1: a mouse model reveals destabilization of cGMP phosphodiesterase. *Proc. Natl. Acad. Sci. U.S.A.* **101,** 13897–13902 CrossRef Medline
18. Liu, X., Bulgakov, O. V., Wen, X. H., Woodruff, M. L., Pawlyk, B., Yang, J., Fain, G. L., Sandberg, M. A., Makino, C. L., and Li, T. (2004) AIPL1, the protein that is defective in Leber congenital amaurosis, is essential for the biosynthesis of retinal rod cGMP phosphodiesterase. *Proc. Natl. Acad. Sci. U.S.A.* **101,** 13903–13908 CrossRef Medline
19. Majumder, A., Gopalakrishna, K. N., Cheguru, P., Gakhar, L., and Artemyev, N. O. (2013) Interaction of aryl hydrocarbon receptor-interacting protein-like 1 with the farnesyl moiety. *J. Biol. Chem.* **288,** 21320–21328 CrossRef Medline
20. Yadav, R. P., Gakhar, L., Yu, L., and Artemyev, N. O. (2017) Unique structural features of the AIPL1–FKBP domain that support prenyl lipid binding and underlie protein malfunction in blindness. *Proc. Natl. Acad. Sci. U.S.A.* **114,** E6536–E6545 CrossRef Medline
21. Yadav, R. P., and Artemyev, N. O. (2017) AIPL1: A specialized chaperone for the phototransduction effector. *Cell Signal.* **40,** 183–189 CrossRef Medline
22. Sokolov, M., Yadav, R. P., Brooks, C., and Artemyev, N. O. (2019) Chaperones and retinal disorders. *Adv. Protein Chem. Struct. Biol.* **114,** 85–117 CrossRef Medline
23. Hidalgo-de-Quintana, J., Evans, R. J., Cheetham, M. E., and van der Spuy, J. (2008) The Leber congenital amaurosis protein AIPL1 functions as part of a chaperone heterocomplex. *Invest. Ophthalmol. Vis. Sci.* **49,** 2878–2887 CrossRef Medline
24. Yadav, R. P., Majumder, A., Gakhar, L., and Artemyev, N. O. (2015) Extended conformation of the proline-rich domain of human aryl hydrocarbon receptor-interacting protein-like 1: implications for retina disease. *J. Neurochem.* **135,** 165–175 CrossRef Medline
25. Schopf, F. H., Biebl, M. M., and Buchner, J. (2017) The HSP90 chaperone machinery. *Nat. Rev. Mol. Cell Biol.* **18,** 345–360 CrossRef Medline
26. Trivellin, G., and Korbonits, M. (2011) AIP and its interacting partners. *J. Endocrinol.* **210,** 137–155 CrossRef Medline
27. Aguilà, M., Bevilacqua, D., McCulley, C., Schwarz, N., Athanasiou, D., Kanuga, N., Novoselov, S. S., Lange, C. A., Ali, R. R., Bainbridge, J. W., Gias, C., Coffey, P. J., Garriga, P., and Cheetham, M. E. (2014) Hsp90 inhibition protects against inherited retinal degeneration. *Hum. Mol. Genet.* **23,** 2164–2175 CrossRef Medline
28. Yu, L., Yadav, R. P., and Artemyev, N. O. (2017) NMR resonance assignments of the FKBP domain of human aryl hydrocarbon receptor-interacting protein-like 1 (AIPL1) in complex with a farnesyl ligand. *Biomol. NMR Assign.* **11,** 111–115 CrossRef Medline
29. Yu, L., Yadav, R. P., and Artemyev, N. O. (2019) NMR resonance assignments of the TPR domain of human aryl hydrocarbon receptor-interacting protein-like 1 (AIPL1). *Biomol. NMR Assign.* **13,** 79–83 CrossRef Medline
30. Artemyev, N. O., and Hamm, H. E. (1992) Two-site high-affinity interaction between inhibitory and catalytic subunits of rod cyclic GMP phosphodiesterase. *Biochem. J.* **283,** 273–279 CrossRef Medline
31. Artemyev, N. O., Rarick, H. M., Mills, J. S., Skiba, N. P., and Hamm, H. E. (1992) Sites of interaction between rod G-protein α-subunit and cGMP-phosphodiesterase γ-subunit: implications for the phosphodiesterase activation mechanism. *J. Biol. Chem.* **267,** 25067–25072 Medline
32. Barren, B., Gakhar, L., Muradov, H., Boyd, K. K., Ramaswamy, S., and Artemyev, N. O. (2009) Structural basis of phosphodiesterase 6 inhibition by the C-terminal region of the γ-subunit. *EMBO J.* **28,** 3613–3622 CrossRef Medline
33. Slep, K. C., Kercher, M. A., He, W., Cowan, C. W., Wensel, T. G., and Sigler, P. B. (2001) Structural determinants for regulation of phosphodiesterase by a G protein at 2.0 A. *Nature* **409,** 1071–1077 CrossRef Medline
34. Morgan, R. M., Hernández-Ramírez, L. C., Trivellin, G., Zhou, L., Roe, S. M., Korbonits, M., and Prodromou, C. (2012) Structure of the TPR domain of AIP: lack of client protein interaction with the C-terminal α-7

helix of the TPR domain of AIP is sufficient for pituitary adenoma predisposition. *PLoS One* **7,** e53339 CrossRef Medline
35. Song, J., Guo, L. W., Muradov, H., Artemyev, N. O., Ruoho, A. E., and Markley, J. L. (2008) Intrinsically disordered γ-subunit of cGMP phosphodiesterase encodes functionally relevant transient secondary and tertiary structure. *Proc. Natl. Acad. Sci. U.S.A.* **105,** 1505–1510 CrossRef Medline
36. Brünger, A. T., Adams, P. D., Clore, G. M., DeLano, W. L., Gros, P., Grosse-Kunstleve, R. W., Jiang, J. S., Kuszewski, J., Nilges, M., Pannu, N. S., Read, R. J., Rice, L. M., Simonson, T., and Warren, G. L. (1998) Crystallography & NMR system: a new software suite for macromolecular structure determination. *Acta Crystallogr. D Biol. Crystallogr.* **54,** 905–921 CrossRef Medline
37. Gulati, S., Palczewski, K., Engel, A., Stahlberg, H., and Kovacik, L. (2019) Cryo-EM structure of phosphodiesterase 6 reveals insights into the allosteric regulation of type I phosphodiesterases. *Sci. Adv.* **5,** eaav4322 CrossRef Medline
38. Ashkenazy, H., Abadi, S., Martz, E., Chay, O., Mayrose, I., Pupko, T., and Ben-Tal, N. (2016) ConSurf 2016: an improved methodology to estimate and visualize evolutionary conservation in macromolecules. *Nucleic Acids Res.* **44,** W344–W350 CrossRef Medline
39. Tsang, S. H., Gouras, P., Yamashita, C. K., Kjeldbye, H., Fisher, J., Farber, D. B., and Goff, S. P. (1996) Retinal degeneration in mice lacking the γ subunit of the rod cGMP phosphodiesterase. *Science* **272,** 1026–1029 CrossRef Medline
40. Tsang, S. H., Woodruff, M. L., Lin, C. S., Jacobson, B. D., Naumann, M. C., Hsu, C. W., Davis, R. J., Cilluffo, M. C., Chen, J., and Fain, G. L. (2012) Effect of the ILE86TER mutation in the γ subunit of cGMP phosphodiesterase (PDE6) on rod photoreceptor signaling. *Cell Signal.* **24,** 181–188 CrossRef Medline
41. Perez-Riba, A., and Itzhaki, L. S. (2019) The tetratricopeptide-repeat motif is a versatile platform that enables diverse modes of molecular recognition. *Curr. Opin. Struct. Biol.* **54,** 43–49 CrossRef Medline
42. Pan, Z., Zhu, J., Shang, Y., Wei, Z., Jia, M., Xia, C., Wen, W., Wang, W., and Zhang, M. (2013) An autoinhibited conformation of LGN reveals a distinct interaction mode between GoLoco motifs and TPR motifs. *Structure* **21,** 1007–1017 CrossRef Medline
43. Huang, D., Hinds, T. R., Martinez, S. E., Doneanu, C., and Beavo, J. A. (2004) Molecular determinants of cGMP binding to chicken cone photoreceptor phosphodiesterase. *J. Biol. Chem.* **279,** 48143–48151 CrossRef Medline
44. Muradov, K. G., Boyd, K. K., Martinez, S. E., Beavo, J. A., and Artemyev, N. O. (2003) The GAFa domains of rod cGMP-phosphodiesterase 6 determine the selectivity of the enzyme dimerization. *J. Biol. Chem.* **278,** 10594–10601 CrossRef Medline
45. Kabsch, W. (2010) XDS. XDS. *Acta Crystallogr. D Biol. Crystallogr.* **66,** 125–132 CrossRef Medline
46. Evans, P. (2006) Scaling and assessment of data quality. *Acta Crystallogr. D Biol. Crystallogr.* **62,** 72–82 CrossRef Medline
47. McCoy, A. J., Grosse-Kunstleve, R. W., Adams, P. D., Winn, M. D., Storoni, L. C., and Read, R. J. (2007) Phaser crystallographic software. *J. Appl. Crystallogr.* **40,** 658–674 CrossRef Medline
48. Murshudov, G. N., Skubák, P., Lebedev, A. A., Pannu, N. S., Steiner, R. A., Nicholls, R. A., Winn, M. D., Long, F., and Vagin, A. A. (2011) REFMAC5 for the refinement of macromolecular crystal structures. *Acta Crystallogr. D Biol. Crystallogr.* **67,** 355–367 CrossRef Medline
49. Adams, P. D., Afonine, P. V., Bunkóczi, G., Chen, V. B., Davis, I. W., Echols, N., Headd, J. J., Hung, L. W., Kapral, G. J., Grosse-Kunstleve, R. W., McCoy, A. J., Moriarty, N. W., Oeffner, R., Read, R. J., Richardson, D. C., *et al.* (2010) PHENIX: a comprehensive Python-based system for macromolecular structure solution. *Acta Crystallogr. D Biol. Crystallogr.* **66,** 213–221 CrossRef Medline
50. Emsley, P., and Cowtan, K. (2004) Coot: model-building tools for molecular graphics. *Acta Crystallogr. D Biol. Crystallogr.* **60,** 2126–2132 CrossRef Medline
51. Mathew, E., Mirza, A., and Menhart, N. (2004) Liquid-chromatography-coupled SAXS for accurate sizing of aggregating proteins. *J. Synchrotron Radiat.* **11,** 314–318 CrossRef Medline
52. Hopkins, J. B., Gillilan, R. E., and Skou, S. (2017) BioXTAS RAW: improvements to a free open-source program for small-angle X-ray scattering data reduction and analysis. *J. Appl. Crystallogr.* **50,** 1545–1553 CrossRef Medline
53. Franke, D., Petoukhov, M. V., Konarev, P. V., Panjkovich, A., Tuukkanen, A., Mertens, H. D. T., Kikhney, A. G., Hajizadeh, N. R., Franklin, J. M., Jeffries, C. M., and Svergun, D. I. (2017) ATSAS 2.8: a comprehensive data analysis suite for small-angle scattering from macromolecular solutions. *J. Appl. Crystallogr.* **50,** 1212–1225 CrossRef Medline
54. Delaglio, F., Grzesiek, S., Vuister, G. W., Zhu, G., Pfeifer, J., and Bax, A. (1995) NMRPipe: a multidimensional spectral processing system based on UNIX pipes. *J. Biomol. NMR* **6,** 277–293 Medline
55. Johnson, B. A., and Blevins, R. A. (1994) NMR View: A computer program for the visualization and analysis of NMR data. *J. Biomol. NMR* **4,** 603–614 CrossRef Medline
56. Sali, A., and Blundell, T. L. (1993) Comparative protein modelling by satisfaction of spatial restraints. *J. Mol. Biol.* **234,** 779–815 CrossRef Medline
57. Svergun, D., Barberato, C., and Koch, M. H. J. (1995) CRYSOL: a program to evaluate x-ray solution scattering of biological macromolecules from atomic coordinates. *J. Appl. Crystallogr.* **28,** 768–773 CrossRef
58. Valentini, E., Kikhney, A. G., Previtali, G., Jeffries, C. M., and Svergun, D. I. (2015) SASBDB, a repository for biological small-angle scattering data. *Nucleic Acids Res.* **43,** D357–D363 CrossRef Medline